Accepted Manuscript

STRUCTURAL AND ELECTROCHEMICAL CHARACTERIZATION OF Zr–C–N- Ag COATINGS DEPOSITED BY DC DUAL MAGNETRON SPUTTERING

S. Calderon Velasco, V. Lopez, C.F. Almeida Alves, A. Cavaleiro, S. Carvalho

Please cite this article as: S. Calderon Velasco, V. Lopez, C.F. Almeida Alves, A. Cavaleiro, S. Carvalho, STRUCTURAL AND ELECTROCHEMICAL CHARACTERIZATION OF Zr–C–N- Ag COATINGS DEPOSITED BY DC DUAL MAGNETRON SPUTTERING, *Corrosion Science* (2013), doi: http://dx.doi.org/10.1016/j.corsci.2013.11.036

STRUCTURAL AND ELECTROCHEMICAL CHARACTERIZATION OF Zr–C–N- Ag COATINGS DEPOSITED BY DC DUAL MAGNETRON SPUTTERING

S. Calderon V[1]; V. Lopez[1]; C. F. Almeida Alves[1]; A. Cavaleiro[2]; S.Carvalho[1]

[1]Physics Department, University of Minho, 4800-058 Guimarães, Portugal.

[2]SEG-CEMUC Mechanical Engineering Department, University of Coimbra, 3030-788 Coimbra, Portugal.

Corresponding author:

Sebastian Calderon Velasco

Universidade do Minho, Dept. Física, Campus de Azurém, 4800-058 Guimarães, Portugal

Tel: +351- 253510175 ext. 517465

Fax: +351-253510461

Email: secave44@gmail.com

ABSTRACT

ZrCN coatings with incorporated silver were deposited on 316L stainless steel by dual reactive magnetron sputtering to evaluate the silver influence on the structural properties and corrosion resistance of the films. Samples composition was assessed by electron probe microanalysis. Glow discharge optical emission spectroscopy was used to determine the distribution of silver in the films. Structural characterization was performed by X-ray diffraction and Raman spectroscopy. Corrosion resistance was evaluated by potentiodynamic test and electrochemical impedance spectroscopy. Results revealed enhanced corrosion resistance properties of the coated steel and higher coatings reactivity when incorporated with silver, showing a plausible silver release increment.

Keywords: A. Ceramic; A. Zirconium; A. Stainless steel; B. EIS; B. XRD; C. anodic films.

INTRODUCTION

Surface engineering is rapidly evolving such that the surface modification of widely used materials allows engineers to convert a material with poor mechanical or corrosion resistance into a functional product in which only few microns or even nanometers have been modified for such purpose. A good example is performed on orthopedic materials used to produce hip, knee or dental prostheses [1-3]. For such application, the coatings are required to be not only chemically stable, in order to produce biocompatible materials, but must also possess good mechanical, tribological and antibacterial properties to prevent implant failure [4]. On this basis, the Me-CN system has been proposed and extensively studied to produce coatings to improve the mechanical and tribological properties of base materials such as SS316L, TiAlV and Ti, among others [5-7]. M. Balaceanu et al. [8], for example, studied ZrCN coatings to optimize the 316L stainless steel protection for medical implants, concluding that an enriched biocompatibility and remodeling process was exhibited, causing a negligible inflammatory response. Lai et al. [9] have demonstrated that the carbon content in ZrCN films, deposited by cathodic-arc evaporation, played a very important role not only on the tribological properties but also on their biocompatibility. They showed that increasing the content of C-based amorphous phase enhances the antibacterial behavior. Furthermore, several reports [10, 11] have established that ZrCN coatings improve the corrosion resistance of the base material in a wide range of fluids. However, little is known about the real ability of ZrCN films to protect the most used prosthetic materials in simulated body fluids.

Some studies have demonstrated that the addition of different elements to ZrCN films can modify and even improve their properties [12-14]. The proper selection of the element may largely enhance the functional properties of the materials, improving mechanical, tribological, chemical and biological behavior.

In this work, the incorporation of silver in the ZrCN matrix is proposed with the final aim to provide this material with additional antibacterial properties, as well as with self-lubrication behavior. The antibacterial properties of silver have been extensively proven in several reports [15-20], related to silver ion release [21-23]. To the authors' knowledge there have not been any publication regarding ZrCN coatings modified with silver. This report aims to expand the state of the art of ZrCN coatings with antibacterial agents, similarly to a current study performed by the authors on the TiCN system [24]. Therefore, in this paper we report the production of ZrCN coatings with silver onto 316L stainless steel, assessing structural changes, as well as electrochemical stability in 8.9 g/L NaCl. The final scope will be to evaluate the viability of this material as a future candidate for biomedical experimentation.

MATERIALS AND METHODS

Coating production

Stainless steel 316L (Fe 68.40 wt. % , Cr 16.40 wt. %, Ni 11.1 wt. %, Mo 2.28 wt. %, Mn 1.3 wt. %, Si 0.39 wt %, P = 0.06 wt. %, and C < 0.03 wt %) with surface roughness of 60 nm (SS316L) (4 cm^2) and Si (100) samples were coated in a reactive DC dual magnetron sputtering chamber with two opposite magnetrons in a close magnetic field configuration, equipped also with a rotatable substrate holder, in order to obtain homogenous deposition conditions, as schematized in Fig. 1. The films were deposited using a pure 99.8% Zr target and a modified 99.8 % Zr target with 6 high-purity silver pellets placed on top of the target surface. The pellets were organized on the erosion zone of the target maintaining a ratio between the Zr and Ag area around 6.5. By varying the current density of the Zr-Ag target, three different silver contents from 0 to 8 at. % were achieved.

The chamber base pressure was set to 7×10^{-4} Pa and thereafter filled with Ar (60 sccm), N_2 (3 sccm) and C_2H_2 (4 sccm) gas to create the proper atmosphere to produce ZrCN films. The working pressure was 0.35 Pa. The gases fluxes, bias voltage (-50 V), substrate rotation speed

(8 rpm) and chamber temperature (100 $^{\circ}$C) were kept constant for all the depositions. Table 1 shows some deposition parameters.

Before each deposition, a custom cleaning procedure was applied to the substrates, using ultrasonic baths in distilled water, ethanol and acetone for 10 min for each solvent, in order to remove dust, impurities and organics from the substrates surfaces and to enhance the films adhesion. Film adhesion was further enhanced by an in situ etching process, immediately before the coatings production, using argon atmosphere and a pulsed power supply. A 50 nm Zr interlayer was deposited before the multifunctional ZrCN-Ag layer to yet further enhance the adhesion of the films to the 316L stainless steel substrates.

Chemical and Physical characterization

The coating chemical composition was analyzed by a Cameca SX 50 electron probe micro-analyzer (EPMA), using statistical analysis of 5 randomly selected spots in each sample. Moreover, the element distribution along the film thickness was evaluated using a glow discharge optical emission spectrometer (GD-OES - Jobin Yvon RF GD Profiler) equipped with a 4 mm diameter anode and operating at a typical radio frequency discharge pressure of 650 Pa and a power of 40 W. GD-OES was mainly utilized to determine qualitatively the distribution of the elements across the films thickness, as an arbitrary intensity and not as a composition percentage.

The structure was studied by X-ray diffraction in a Siemens diffractometer with Co Kα (1.78897) radiation in a grazing angle mode.

Topography and morphology of the films was evaluated on samples deposited onto Si wafers by atomic force microscopy in contact mode (area of 5 µm X 5 µm), using a NanoScope III Digital Instruments atomic force microscope. The cross section morphology of the films and their thickness were assessed using a NanoSEM - FEI Nova 200 scanning electron microscope, with a secondary electron detector.

Finally, further structural analysis was performed by Raman spectroscopy with a Renishaw InVia Microscope with an excitation light of Ar 514.5 nm laser.

Corrosion Tests

The corrosion behavior was assessed by electrochemical impedance spectroscopy (EIS) and anodic potentiodynamic polarization. The tests were performed with a Gamry REF600 potentiostat on the bare and coated 316L stainless steel substrates using a classic corrosion cell with platinum and saturated calomel (SCE) as counter and reference electrodes, respectively. The samples were immersed into a simulated body fluid (0.89 wt. % NaCl) at 37 °C with stabilized pH (7.0-7.5). Before each impedance spectrum, a stable OCP potential was achieved during 1 h and a sinusoidal AC perturbation of 10 mV (rms) amplitude around the corrosion potential was applied to the electrode over the frequency range 0.01 Hz– 100 kHz. Thereafter, potentiodynamic tests were performed using a scanning rate of 60 mV/min from -500 mV vs. OCP to +1800 mV vs. OCP.

RESULTS AND DISCUSSION

Physical and chemical characterization

Table 1 shows the experimental conditions, chemical composition and some physical properties of the films. The deposition rate is reduced by increasing the silver content on the films, despite the fact that the current density to the targets was kept at 10 mA/cm^2. The difference in silver content was attained by increasing the current density in the Zr-Ag target and decreasing the Zr target current density proportionally, as shown in Table 1. Thus, considering the amount of silver that replaces Zr in the erosion zone of the Zr-Ag target (15.5%), it is evident that despite the fact that silver possesses a higher sputtering yield than Zr-compounds, it does not lead to an increase in the deposition rate. This fact is explained due to a reduction of the total power during each deposition, as observed in table 1.

Table 1 also depicts the evolution of the chemical composition as a function of the current density ratio (Zr-Ag/Zr) applied to the targets. The incorporation of silver in the film led to a decrease in the Zr content to almost 14 at. %, as would be expected since the silver is replacing a certain area of Zr in the Zr-Ag target erosion zone. Thus, a decrease of the zirconium content in the films was found to exhibit a linear correlation as a function of the silver content and carbon content with R-square close to 0.983 and 0.997, respectively. This linear behavior is due to the fact that the Zr and silver contents change linearly with the current density and the power applied to each target. The decrease of Zr sputtered from the target will promote its preferential bonding with nitrogen rather than with carbon atoms, which are existing in the same proportion in the atmosphere as in the deposition of the coating without Ag, since the enthalpy of formation of ZrN and ZrC are close to -367.52 kJ/mol [25] and -170.50 kJ/mol [26], respectively. This deficiency of Zr and the excess of C-containing species in the reactive atmosphere leave more carbon atoms to bond to each other and form C-based amorphous phase. This behavior is also expressed in terms of the (C+N)/Zr ratio which is increasing as a function of the Ag content, reaching values (~3) that are not compatible with the formation of a Zr compound, even given that sputtering technique easily allows deposition of over-stoichiometric compounds. As a result, a larger portion of amorphous phases (a:C or C:N phases) should be expected in the final deposited coating.

Additionally to Zr, C, N and Ag, some oxygen content was detected in the films resulting from contamination of the targets and residual oxygen in the chamber atmosphere.

The in-depth silver profile of the films obtained by GD-OES is shown in Fig. 2. Homogeneous Ag content was observed throughout the film, excluding the top surface. Therefore, only the first 150 nm are shown in the figure in order to be able to observe details on the surface. Segregation of silver in the top 10 nm of the film is detected. This redistribution has been also observed by Mulligan et al. [27] after thermal treatment of CrN-Ag films in which films with higher silver content exhibits surface segregation due to the increase of the silver mobility.

Thus, this segregation may be due to the rise of the silver mobility promoted by the increase in the target current density applied for films with higher Ag content.

XRD analysis (Fig. 3) reveals a typical ZrN(C) face center cubic (FCC) crystalline structure with a B1 NaCl type, typical of many transition metal nitrides and carbides [28]. The incorporation of silver in the system decreases the degree of crystallinity with a loss of peaks intensities as well as broader peaks indicating smaller grains (Table 1). Furthermore, despite the incorporation of silver, no peak identifying the silver crystalline structure is undoubtedly defined, revealing that very low grain sizes should occur for the silver. However, a closer look to the XRD peaks of the ZrN(C) phase showed an asymmetric left tail for both 4 at. % and 8 at. % of silver, in positions assigned to silver with a FCC structure, as shown in the inset of figure 3. This observation suggests that silver clusters exist in the coatings.

The sample with 8 at. % of silver also revealed Zr peaks from the interlayer with a BCC crystalline structure, which can be explained due to the lower thickness of this film. In addition, the sample with 8 at. % of silver showed a slight shift to lower angles in the ZrCN phase, which may suggest loss of oxygen in the ZrCN lattice due to the reduction of this element as Zr is reduced.

The grain size of the ZrCN phase was calculated by the Scherrer formula [29] considering the most intense peak of the spectra (111). A decrease of the grain size from 14.3 nm to 2.5 nm is achieved when silver is augmented. The decrease in the grain size may be explained by the influence of silver nanoparticles and the amorphous phase that increase the nucleation rate of ZrN(C) and prevent the grain growth.

Raman spectroscopy confirmed the presence of C-based amorphous phase. The spectra shown in Fig. 4 represent the Raman shift of the samples and their dependence on the silver content. The C-C bonds located at 1336 cm^{-1} and 1570 cm^{-1}, corresponding to the D (disordered) and G (graphitic) bands of disordered carbon, confirm the presence of the amorphous carbon phase in the films [12]. The ratio between the intensities of these peaks could represent the degree of

disorder of the amorphous phase in the system; however, the D/G ratio was calculated to be constant for both Ag contents, revealing similar structures and sp2 and sp3 C bond contents in the coatings.

On the other hand, ZrN forbidden bands (the first order Raman scattering) are observed due to the disorder and imperfection of the structure caused by oxygen and carbon atoms in the lattice [30]. Constable [31] reported the presence of two bands; one due to the acoustic transition (173,241 cm^{-1}) and the other to optic modes (473-580 cm^{-1}). These four peaks are observed in the ZrN(C) films, while their presence is diminished for samples with silver due to the reduction of Zirconium and oxygen in this phase decreasing the presence of this phase in the material, as observed in the XRD results.

Morphology

All films exhibit similar morphological features. Fig. 5 shows surface and cross-section SEM micrographs of the samples. The images reveal films densification as silver is introduced. This densification is not only due to the silver effect in the grain size but also due to the increase of amorphous carbon phases in the films. All the films experienced columnar growth in which the columns are not very well defined, characteristic of the zone T in the model described by Thornton [32]. This zone is characterized by a dense array with poorly defined fibrous grains. Furthermore, this zone is characterized by a smooth surface morphology, as confirmed by AFM measurements, showing low roughness of the films (Table 1). The roughness showed a reduction for films with silver, highly influenced by the reduction of grain and column size promoted by the amorphous phases and the silver segregation.

Surface images also revealed presence of small bright spots for the sample with highest silver content; these bright dots are probably silver nanoparticles that confirm GD-OES agglomeration of silver on the surface of such sample.

Corrosion Behavior

Table 2 shows the open circuit potential (OCP), corrosion potential (E$_{corr}$) and breakdown potential (E$_b$) of SS316L and ZrCN-Ag samples immersed in 8.9 g/l NaCl at 37 °C. OCP values

reveal that ZrCN without silver presents lower potentials compared with the bare stainless steel, while higher values are measured when silver is introduced in the system. This increase is probably due to the increment of a:C phases and silver metallic that compared with ZrCN exhibit higher corrosion potentials [33, 34], and therefore the mixed corrosion potential of the system is increased.

The potentiodynamic curves shown in Fig. 6 reveal that all the films enhance the corrosion resistance of the bare stainless steel. Pitting or localized corrosion registered a similar trend, except for the film with 4 at. % of silver, for which the E_b occurs at similar potentials as for SS316L and the difference between E_b and E_{corr} is the lowest among all the studied samples, revealing a less protective material for polarization induced corrosion. The plot also displays a shift to lower current after SS316L is coated, regardless the amount of silver. This shift is related with the kinetic of the corrosion mechanism, signifying a reduced corrosion rate of the coatings. However, only slight differences are noticed in the polarization curves of the coatings. The most significant difference is noticed for the films with 8 at. % of silver, in which the anodic branch of the curve has a different slope, indicating greater changes of the current with small potential variations. This change may indicate more reactive material which is likely due to the presence of silver nanoparticles. Thus, while the current increment indicates the films potential for working as antibacterial agent by releasing more silver, the coated material is only marginally affected in its corrosion resistance without reaching the SS316L levels of corrosion current.

Electrochemical impedance spectroscopy was performed to characterize in more detail the corrosion behavior of the films. Fig. 7 shows the Bode plots for all the samples, as well as for the bare stainless steel. All samples showed a capacitive behavior, reflected in the phase angle curves. However, the SS316L measurements showed maximum phase angles closer to 90 degrees, which represent more pure capacitive response for higher frequency values. Nonetheless, despite the fact that the phase angle values were lower for the films, they are maintained in a larger range of frequencies, probably indicating low penetration of the

electrolyte. The phase vs frequency plot for the SS316L and 0 and 4 % of silver displays a simple structure that indicates a single time constant while the 8 at. % of silver seems to have the presence of more than one time constant.

Based on this analysis, the results were fitted using the equivalent circuits shown in Fig. 8, in which the capacitance element is replaced by a constant phase element in order to consider the surface roughness and heterogeneities [35-37] and the R_p represents the polarization resistance element, which represents the charge transference resistance of the material. Sample with 8 at. % of silver was fitted using the same model since the use of a more complex model did not reveal any improvement in the fitting parameter, and therefore, the non-Faradic and Faradic interfacial processes are described by double layer capacitance and the polarization resistance of the films, respectively.

Table 3 shows the results obtained after fitting EIS data. Parameter Y_o cannot be considered to represent the double layer capacitance of the system since it depends on the α parameter. Thus, it is necessary to correlate them by means of a relationship proposed by Brug et al. [38] to obtain an effective capacitance (C_{eff}). This C_{eff} shows a constant reduction as a function of the silver content in the ZrCN films (Fig. 9). The decrease of the double layer capacitance may indicate a decrease of an oxide layer formed naturally on the surface of material in contact with the environment [28] and is reduced due to the incorporation of the silver and the appearance of a nanometric silver layer revealed by GD-OES. This oxide layer is likely to be formed in this type of materials but very poor blocking ability is expected [39].

The charge transference resistance, on the other hand, revealed an enhanced corrosion behavior for the coated SS316L compared with the uncoated steel. However, the increment of the metallic phase (Ag) in the material induces a reduction on the polarization resistance of the material. The reduction of the Rp parameter, plotted in Fig. 9, may be explained due to a combination of three main consequences induced by the introduction of the silver. Firstly, the addition of a metallic material is expected to be more electrochemical active compared with a

ceramic ZrCN solid solution, which in turn supports the use of silver as an antibacterial agent embedded into this matrix. Nonetheless, silver segregation on the surface, forming a thin film (10 nm) richer in silver, is observed as Ag increases (Fig. 2), probably explaining the more active electrochemical behavior of sample with higher silver content compared with the substrate. Secondly, the samples structural characterization revealed that silver induces a grain size diminution of the ZrCN cabonitride phase due to the creation of nucleation points for such phase, and hence, increasing the amount of grain boundaries, causing more unstable sites in which corrosion may occur , reflected in a lower polarization resistance of the system, as shown in Fig. 10a. Thirdly, although amorphous carbon phases are electrochemically nobler than the substrate, the introduction of such phases into the films promotes the formation of more diffusion paths throughout the grain boundaries in the films that can lead to electrochemical dissolution of the substrates due to permeation of the electrolyte, damaging the corrosion resistant of the films.

CONCLUSION

ZrCN films with 0, 4 and 8 at. % of silver, were successfully deposited by dual reactive magnetron sputtering. Crystalline phase analysis revealed a diminution of ZrN(C) grain size and an increment of the C-based amorphous phases associated to the decrease of the Zr/(C+N) atomic ratio [40] induced by the incorporation of silver into the films. Denser coatings were obtained by increasing the Zr-Ag targets current density, primary explained due to the silver and amorphous phases incorporation, affecting the grain and column size of the coatings, while the topographical analysis suggests a reduction on the surface roughness influenced by silver. Finally, electrochemical assays showed enhanced corrosion resistance compared to the SS316L for films with low content of silver. However, for 8 at. % of silver the polarization resistance of the films was reduced below the steel polarization resistance which may indicate very electrochemical active silver. The system can be incorporated with silver to confer the aimed

antibacterial and self-lubricant properties, keeping or slightly improving the corrosion resistance

properties of the base system.

ACKNOWLEDGEMENTS

REFERENCES

[1] R.A. Antunes, A.C.D. Rodas, N.B. Lima, O.Z. Higa, I. Costa, Study of the corrosion resistance and in vitro biocompatibility of PVD TiCN-coated AISI 316 L austenitic stainless steel for orthopedic applications, Surface and Coatings Technology, 205 (2010) 2074-2081.
[2] W. Österle, D. Klaffke, M. Griepentrog, U. Gross, I. Kranz, C. Knabe, Potential of wear resistant coatings on Ti–6Al–4V for artificial hip joint bearing surfaces, Wear, 264 (2008) 505-517.
[3] H.C. Hsu, S.K. Yen, Evaluation of metal ion release and corrosion resistance of ZrO2 thin coatings on the dental Co–Cr alloys, Dental Materials, 14 (1998) 339-346.
[4] L. Mattei, F. Di Puccio, B. Piccigallo, E. Ciulli, Lubrication and wear modelling of artificial hip joints: A review, Tribology International, 44 (2011) 532-549.
[5] E. Silva, M. Rebelo de Figueiredo, R. Franz, R. Escobar Galindo, C. Palacio, A. Espinosa, S. Calderon V, C. Mitterer, S. Carvalho, Structure-property relations in ZrCN coatings for tribological applications, Surface and Coatings Technology, 205 (2010) 2134-2141.
[6] K.T. Rie, J. Wöhle, Plasma-CVD of TiCN and ZrCN films on light metals, Surface and Coatings Technology, 112 (1999) 226-229.
[7] S. Kudapa, K. Narasimhan, P. Boppana, W. Russell, Characterization and properties of MTCVD TiCN and MTCVD ZrCN coatings, Surface and Coatings Technology, 120 (1999) 259-264.
[8] M. Balaceanu, T. Petreus, V. Braic, C. Zoita, A. Vladescu, C. Cotrutz, M. Braic, Characterization of Zr-based hard coatings for medical implant applications, Surface and Coatings Technology, 204 (2010) 2046-2050.
[9] C.H. Lai, Y.Y. Chang, H.L. Huang, H.Y. Kao, Characterization and antibacterial performance of ZrCN/amorphous carbon coatings deposited on titanium implants, Thin Solid Films, 520 (2011) 1525-1531.
[10] J.D. Gu, P.L. Chen, Investigation of the corrosion resistance of ZrCN hard coatings fabricated by advanced controlled arc plasma deposition, Surface and Coatings Technology, 200 (2006) 3341-3346.
[11] K.T. Rie, A. Gebauer, J. Wöhle, Plasma assisted CVD for low temperature coatings to improve the wear and corrosion resistance, Surface and Coatings Technology, 86–87, Part 2 (1996) 498-506.

[12] M. Braic, V. Braic, M. Balaceanu, A. Vladescu, C. Zoita, I. Titorencu, V. Jinga, (Zr, Ti) CN coatings as potential candidates for biomedical applications, Surface and Coatings Technology, 206 (2011) 604-609.

[13] M. Braic, M. Balaceanu, A. Vladescu, C.N. Zoita, V. Braic, Study of (Zr,Ti)CN, (Zr,Hf)CN and (Zr,Nb)CN films prepared by reactive magnetron sputtering, Thin Solid Films, 519 (2011) 4092-4096.

[14] C.M. Cotrut, M. Balaceanu, I. Titorencu, V. Braic, M. Braic, ZrNbCN thin films as protective layers in biomedical applications, Surface and Coatings Technology, 211 57-61.

[15] A. Betts, D. Dowling, M. McConnell, C. Pope, The influence of platinum on the performance of silver-platinum anti-bacterial coatings, Materials & design, 26 (2005) 217-222.

[16] A.M. El-Kady, A.F. Ali, R.A. Rizk, M.M. Ahmed, Synthesis, characterization and microbiological response of silver doped bioactive glass nanoparticles, Ceramics International, 38 (2011) 177-188.

[17] C.N. Lok, C.M. Ho, R. Chen, Q.Y. He, W.Y. Yu, H. Sun, P.K.H. Tam, J.F. Chiu, C.M. Che, Silver nanoparticles: partial oxidation and antibacterial activities, Journal of Biological Inorganic Chemistry, 12 (2007) 527-534.

[18] P. Kelly, H. Li, P. Benson, K. Whitehead, J. Verran, R. Arnell, I. Iordanova, Comparison of the tribological and antimicrobial properties of CrN/Ag, ZrN/Ag, TiN/Ag, and TiN/Cu nanocomposite coatings, Surface and Coatings Technology, 205 (2010) 1606-1610.

[19] H. Cao, X. Liu, F. Meng, P.K. Chu, Biological actions of silver nanoparticles embedded in titanium controlled by micro-galvanic effects, Biomaterials, 32 (2011) 693-705.

[20] D. Dowling, A. Betts, C. Pope, M. McConnell, R. Eloy, M. Arnaud, Anti-bacterial silver coatings exhibiting enhanced activity through the addition of platinum, Surface and Coatings Technology, 163 (2003) 637-640.

[21] K. Jamuna-Thevi, S. Bakar, S. Ibrahim, N. Shahab, M. Toff, Quantification of silver ion release, in vitro cytotoxicity and antibacterial properties of nanostuctured Ag doped TiO2 coatings on stainless steel deposited by RF magnetron sputtering, Vacuum, 86 (2011) 235-241.

[22] S. Sant, K. Gill, R. Burrell, Nanostructure, dissolution and morphology characteristics of microcidal silver films deposited by magnetron sputtering, Acta biomaterialia, 3 (2007) 341-350.

[23] J. Hsieh, C. Tseng, Y. Chang, S. Chang, W. Wu, Antibacterial behavior of TaN–Ag nanocomposite thin films with and without annealing, Surface and Coatings Technology, 202 (2008) 5586-5589.

[24] N. Manninen, R.E. Galindo, N. Benito, N. Figueiredo, A. Cavaleiro, C. Palacio, S. Carvalho, Ag–Ti (C, N)-based coatings for biomedical applications: influence of silver content on the structural properties, Journal of Physics D: Applied Physics, 44 (2011) 375501.

[25] X. Ma, C. Li, K. Bai, P. Wu, W. Zhang, Thermodynamic assessment of the Zr–N system, Journal of alloys and compounds, 373 (2004) 194-201.

[26] F.B. Baker, E.K. Storms, C.E. Holley Jr, Enthalpy of formation of zirconium carbide, Journal of Chemical and Engineering Data, 14 (1969) 244-246.

[27] C. Mulligan, D. Gall, CrN–Ag self-lubricating hard coatings, Surface and Coatings Technology, 200 (2005) 1495-1500.

[28] S.C. V, R.E. Galindo, N. Benito, C. Palacio, A. Cavaleiro, S. Carvalho, Ag+ release inhibition from ZrCN–Ag coatings by surface agglomeration mechanism: structural characterization, Journal of Physics D: Applied Physics, 46 (2013) 325-303.

[29] D.M. Smilgies, Scherrer grain-size analysis adapted to grazing-incidence scattering with area detectors, Journal of Applied Crystallography, 42 (2009) 1030-1034.

[30] C. Moura, P. Carvalho, F. Vaz, L. Cunha, E. Alves, Raman spectra and structural analysis in ZrO< sub> x</sub> N< sub> y</sub> thin films, Thin Solid Films, 515 (2006) 1132-1137.

[31] C.P. Constable, J. Yarwood, W.D. Münz, Raman microscopic studies of PVD hard coatings, Surface and Coatings Technology, 116–119 (1999) 155-159.

[32] J.A. Thornton, High Rate Thick Film Growth, Annual Review of Materials Science, 7 (1977) 239-260.

[33] D. Turcio-Ortega, S.E. Rodil, S. Muhl, Corrosion behavior of amorphous carbon deposit in 0.89% NaCl by electrochemical impedance spectroscopy, Diamond and Related Materials, 18 (2009) 1360-1368.

[34] J.F. Dante, J. Averett, F. Friedersdorf, C. Vestal, L. Innovations, Accelerated corrosion testing of galvanic couples, in: DoD Corrosion Conference, Department of Defense, USA, 2009.

[35] C. Liu, Q. Bi, A. Leyland, A. Matthews, An electrochemical impedance spectroscopy study of the corrosion behaviour of PVD coated steels in 0.5 N NaCl aqueous solution: Part II.: EIS interpretation of corrosion behaviour, Corrosion Science, 45 (2003) 1257-1273.

[36] G. Ramírez, S. Rodil, S. Muhl, D. Turcio-Ortega, J. Olaya, M. Rivera, E. Camps, L. Escobar-Alarcón, Amorphous niobium oxide thin films, Journal of Non-Crystalline Solids, 356 (2010) 2714-2721.

[37] S.L.d. Assis, S. Wolynec, I. Costa, Corrosion characterization of titanium alloys by electrochemical techniques, Electrochimica Acta, 51 (2006) 1815-1819.

[38] G.J. Brug, A.L.G. van den Eeden, M. Sluyters-Rehbach, J.H. Sluyters, The analysis of electrode impedances complicated by the presence of a constant phase element, Journal of Electroanalytical Chemistry and Interfacial Electrochemistry, 176 (1984) 275-295.

[39] P. Pedrosa, E. Alves, N.P. Barradas, P. Fiedler, J. Haueisen, F. Vaz, C. Fonseca, TiNx coated polycarbonate for bio-electrode applications, Corrosion Science, 56 (2012) 49-57.

[40] M.M. Larijani, M.B. Zanjanbar, A. Majdabadi, The effect of carbon fraction in Zr(C, N) films on the nano-structural properties and hardness, Journal of alloys and compounds, 492 (2010) 735-738.

Figure Captions

Figure 1 Dual magnetron sputtering chamber configuration scheme used for the deposition of Zr-C-N-Ag coatings.

Figure 2 silver depth profiles of Zr-C-N-Ag coatings with different silver content obtained by GD-OES.

Figure 3 X-ray diffraction diffractograms of Zr-C-N-Ag coatings with different silver content. Inset: Zoom between 42.2 and 48 degrees for ZrCN with 4 at. % of silver.

Figure 4 Raman spectra of Zr-C-N-Ag coatings with different silver content.

Figure 5 SEM micrographs of a) Zr-C-N-Ag with 0 at. % of Ag surface deposited on SS316L, b) Zr-C-N-Ag with 0 at. % of Ag cross section deposited on Si, c) Zr-C-N-Ag with 4 at. % of Ag surface deposited on SS316L, f) Zr-C-N-Ag with 4 at. % of Ag cross section deposited on Si, e) Zr-C-N-Ag with 0 at. % of Ag surface deposited on SS316L and f) Zr-C-N-Ag with 8 at. % of Ag cross section deposited on Si.

Figure 6 Potentiodynamic curves of Zr-C-N-Ag coatings with different silver concentration using 8.9 g/L NaCl as electrolyte at 37 °C.

Figure 7 Bode plot of the bear SS316L and coated with Zr-C-N-Ag coatings with different silver contents using 8.9 g/l NaCl as electrolyte at 37 °C. Measured (open dots) and fitted (lines) values of the impedance module are related to the left axis while the measured (close dots) and fitted (lines) values of phase are related to the right axis.

Figure 8 Equivalent circuit model scheme used for fitting the EIS data. The R_{sol} represents the resistance due to the electrolyte, R_p is the charge transference resistance also known as polarization resistance, CPE is the phase constant element replacing the double lager capacitance usually utilized to take into consideration the frequency dispersion observed due to surface characteristics.

Figure 9 Zr-C-N-Ag films polarization resistance (o) and effective capacitance (Δ) as a function of the silver content.

Figure 10 Zr-C-N-Ag films polarization resistance (o) and effective capacitance (Δ) as a function of a) the ZrCN grain size and b) the ratio between the carbon, nitrogen and zirconium content ((C+N)/Zr).

Table 1. Deposition parameters, chemical composition and physical properties.

Sample	Working Preassure (Pa)	Base Pressure (1x10^{-4}Pa)	J$_{Zr}$(A/cm^2)	J$_{Zr+Ag}$ (A/cm^2)	Zr Potential (V)	Zr-Ag Potential (V)	Zr Power (W)	Zr-Ag Power (W)	Thickness (nm)	Deposition Rate (µm/h)	Zr C N Grain Size (111)	Roughness (nm)	Composition (at. %)				
													Zr	C	N	O	Ag
0 %	0.36	7.3	10	0	380	0	770	0	813	2.4 ± 0.1	14.3	7.1 ± 1.6	36.4	37.1	18.6	7.9	0
4 %	0.39	7.14	7.5	2.5	365	340	550	170	675	2.0 ± 0.1	6.1	3.3 ± 0.3	28.0	41.8	20.9	5.3	4.0
8 %	0.39	7.6	5	5	365	350	365	356	660	2.0 ± 0.1	2.5	3.2 ± 0.6	20.8	46.7	21.0	3.5	8.0

The compositions presented in the table possess standard deviation between 0.11 and 0.75.

Table 2. Open circuit potential, corrosion potential and breakdown potential of SS316L and ZrCN-Ag samples immersed in 8.9 g/l NaCl at 37 °C. The results are standard deviations calculated based on experimental results of three separate samples.
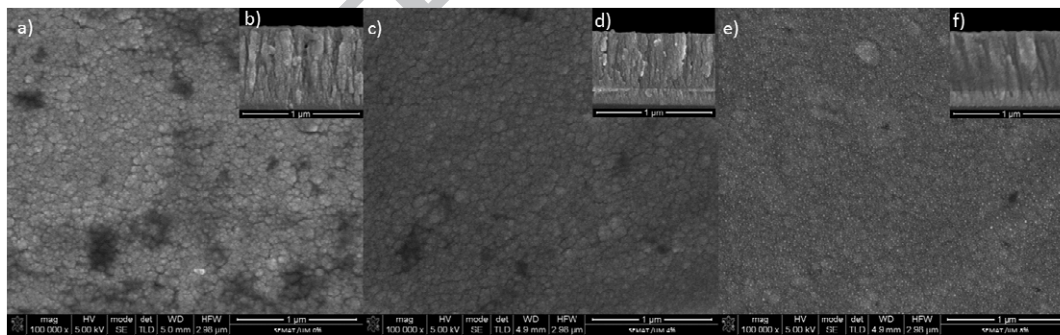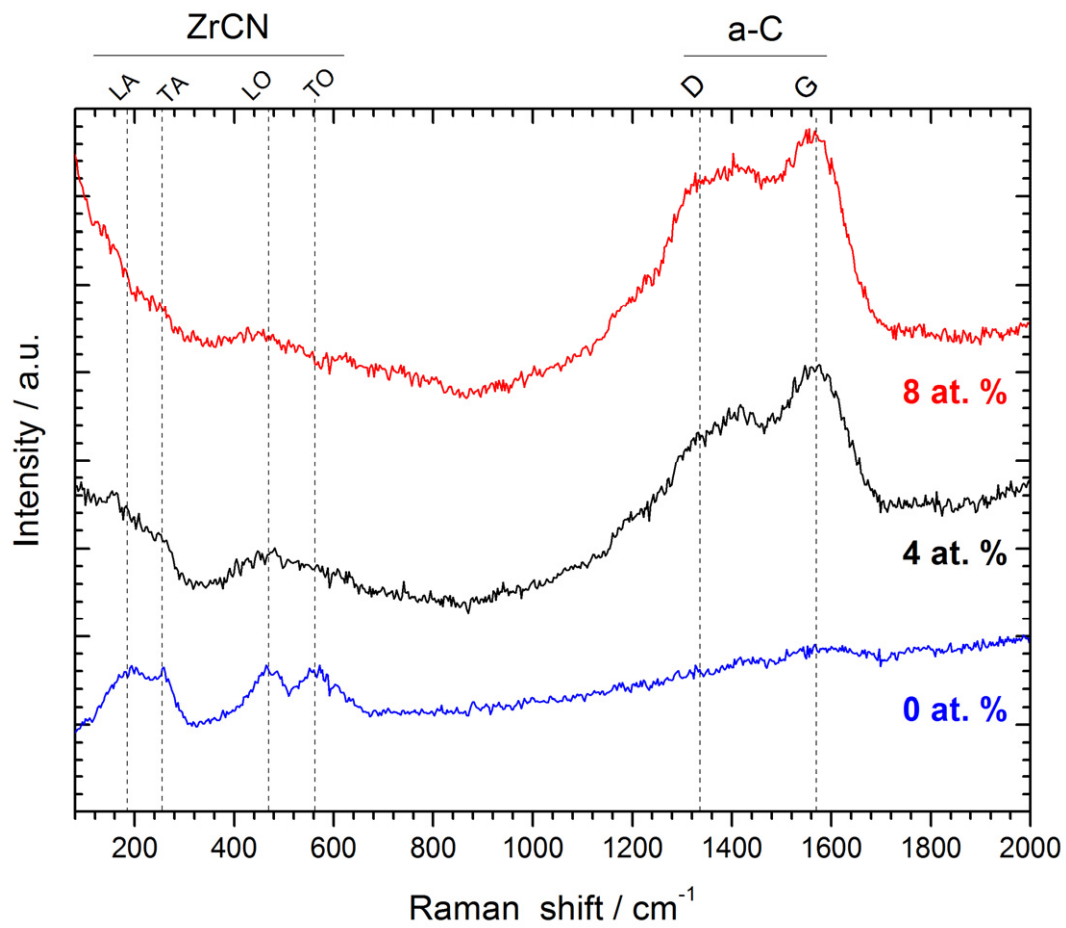
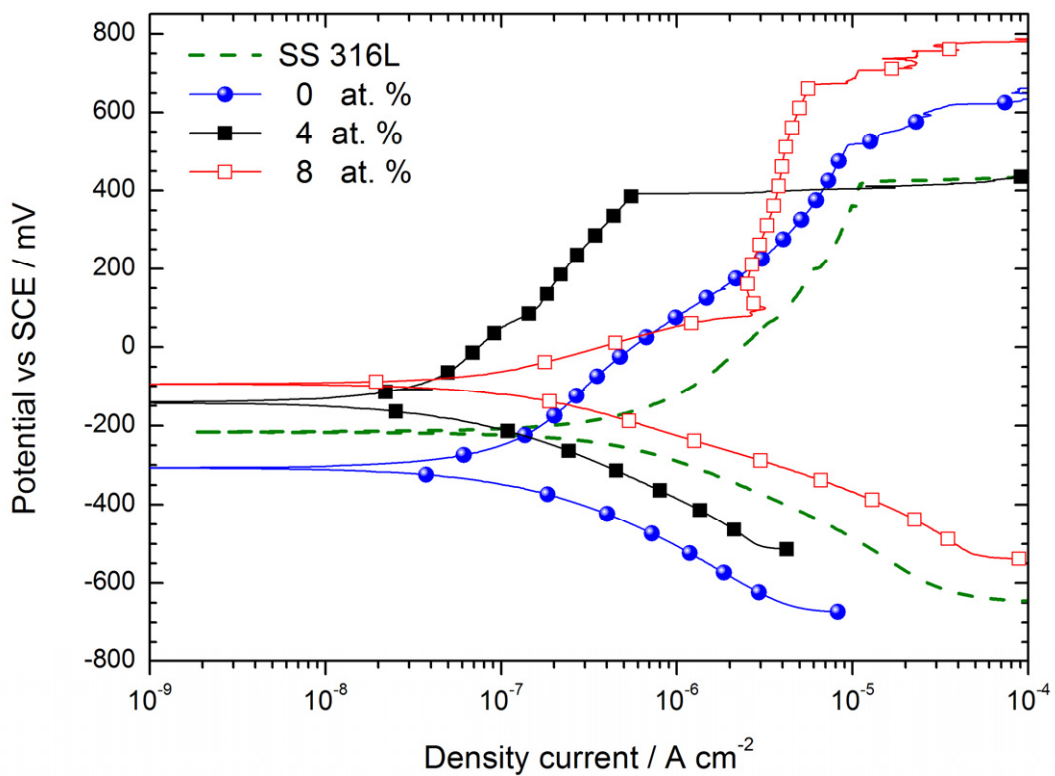| Silver Content (at. %)	OCP vs SCE(mV)		E_{corr} vs SCE(mV)		E_b vs SCE(mV)	
SS 316L	-144.1	± 6.8	-178	± 10.0	396.4	± 20.0
0	-194.2	± 19.3	-322.5	± 15.9	492.0	± 38.2
4	-29.0	± 8.5	-136.7	± 2.5	430.7	± 23.8
8	-28.6	± 8.3	-98.9	± 5.7	745.3	± 66.0

Table 3. EIS fitting parameters for SS316L and ZrCN-Ag coatings in 8.9 % NaCl at 37 C. The results are standard deviations calculated based on experimental results of three separate samples.
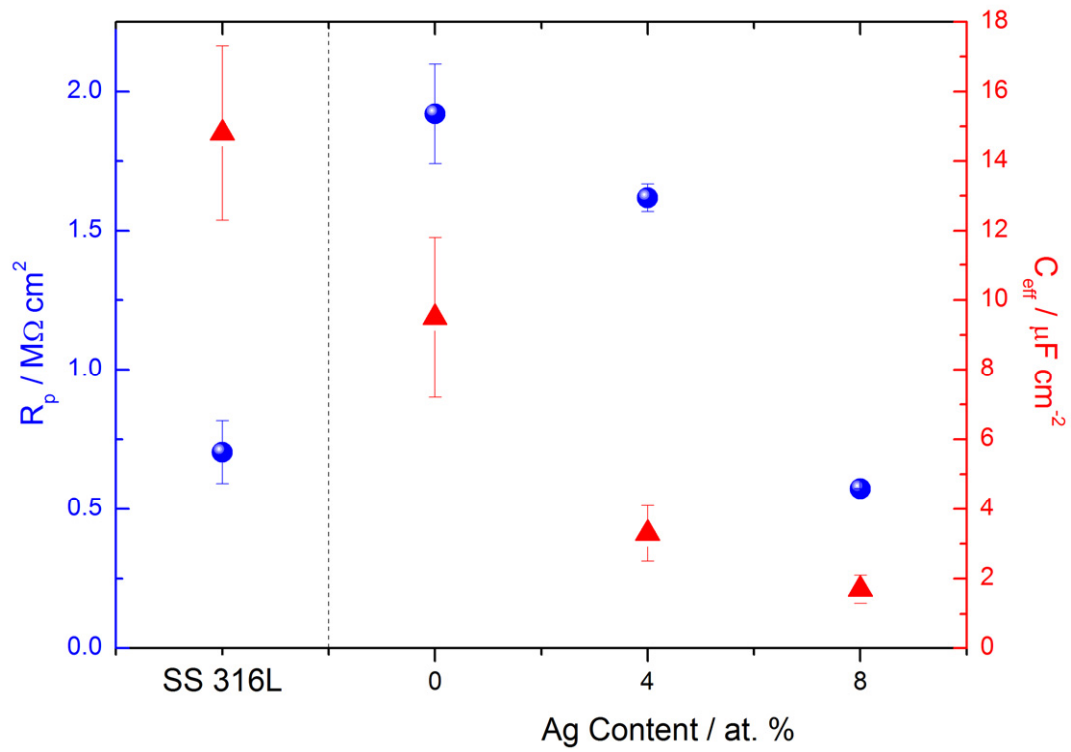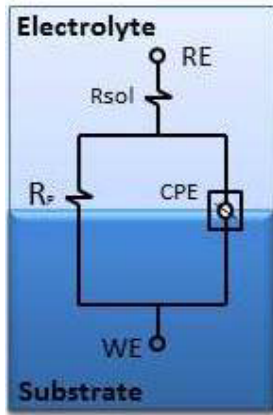
Silver Content (at. %)	$R_{sol}(\Omega\ cm^2)$	$R_p(k\Omega cm^2)$	$Y_o(\mu S\ s^\alpha cm^{-2})$	α	$C_{eff}(\mu F\ cm^{-2})$
SS316L	34.2 ± 2.5	703.8 ± 112.2	29.0 ± 1.3	0.912 ± 0.019	14.8 ± 2.5
0	30.0 ± 0.5	1919.7 ± 179.7	48.6 ± 0.9	0.800 ± 0.003	9.5 ± 2.3
4	36.4 ± 1.5	1618 ± 49.5	19.1 ± 1.7	0.807 ± 0.002	3.3 ± 0.8
8	25.9 ± 0.8	573.32 ± 0.9	28.2 ± 4.9	0.718 ± 0.004	1.7 ± 0.4

a)

Ag at. %

0 at. %

4 at. %

8 at. %

R_p / MΩ cm^2

C_{eff} / μF cm^{-2}

ZrCN grain size / nm

b)

Ag at. %

0 at. %

4 at. %

8 at. %

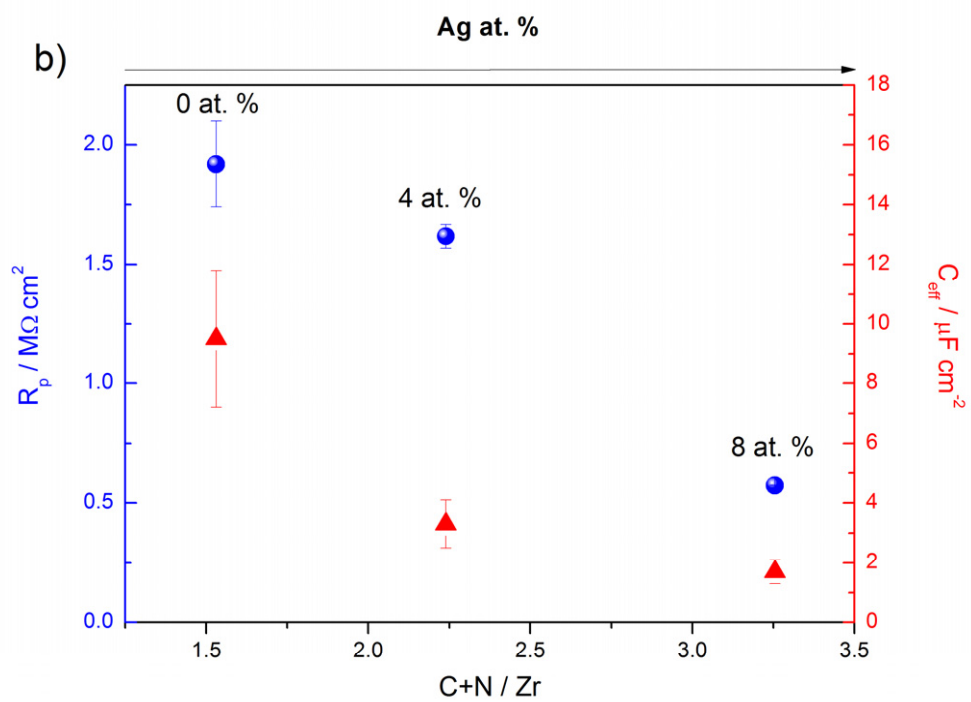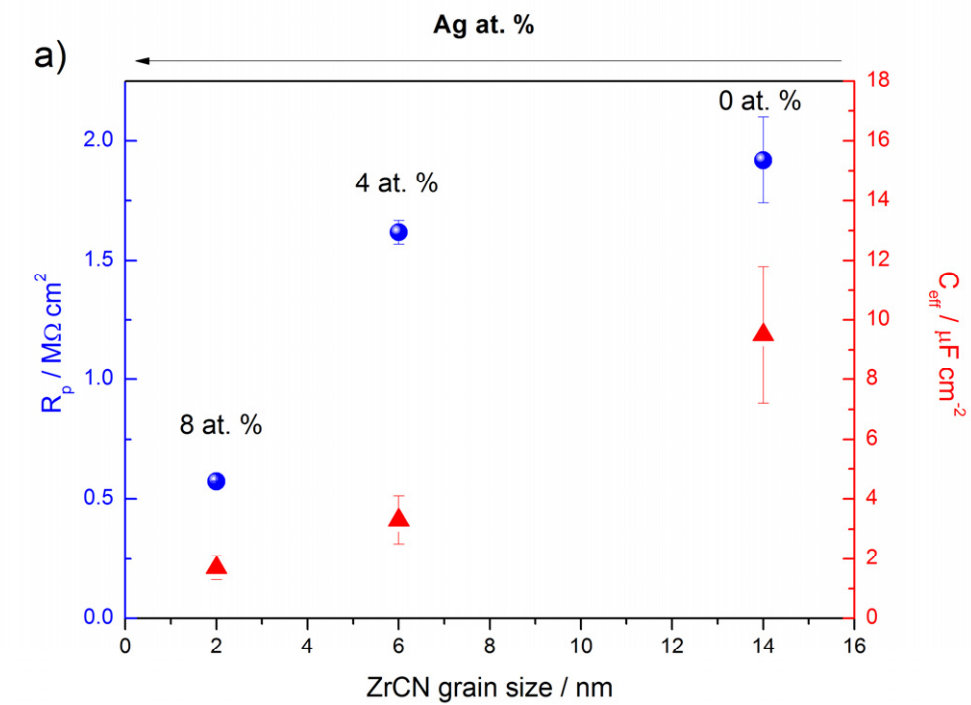R_p / MΩ cm^2

C_{eff} / μF cm^{-2}

C+N / Zr
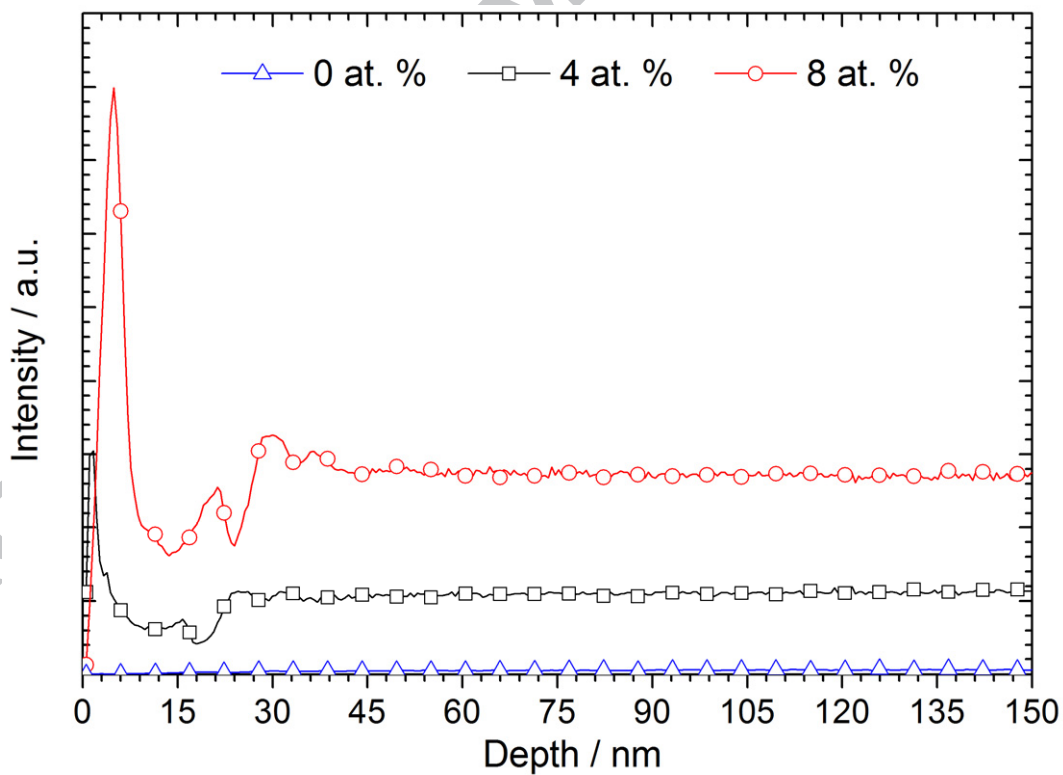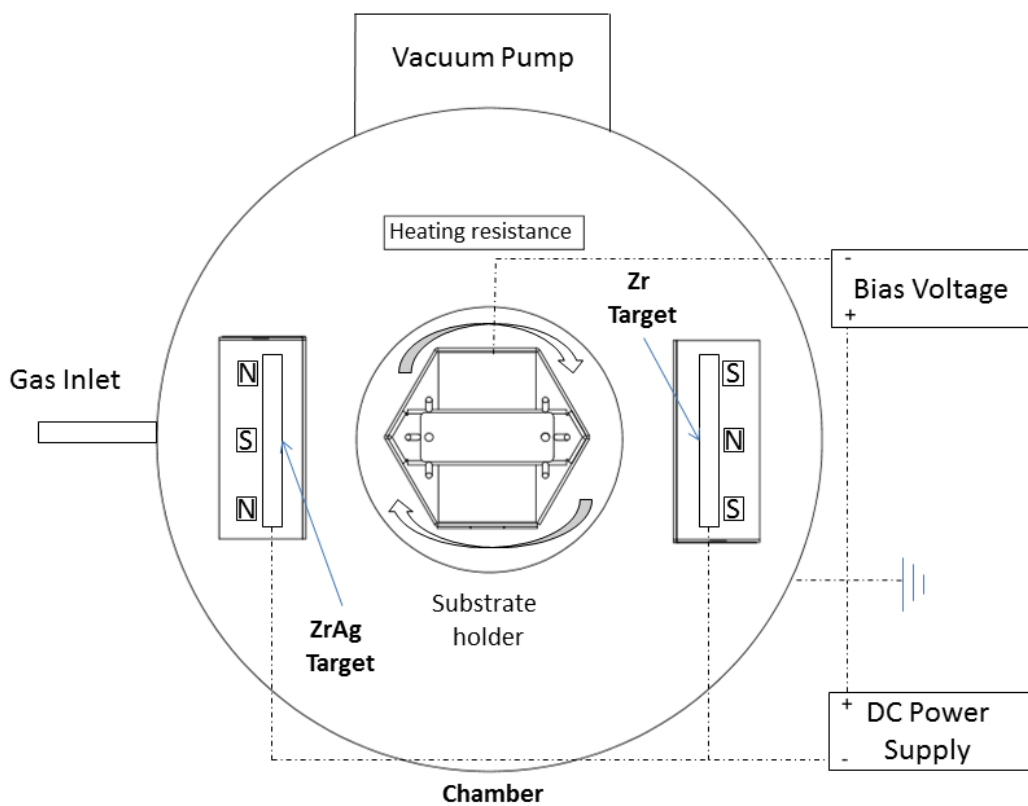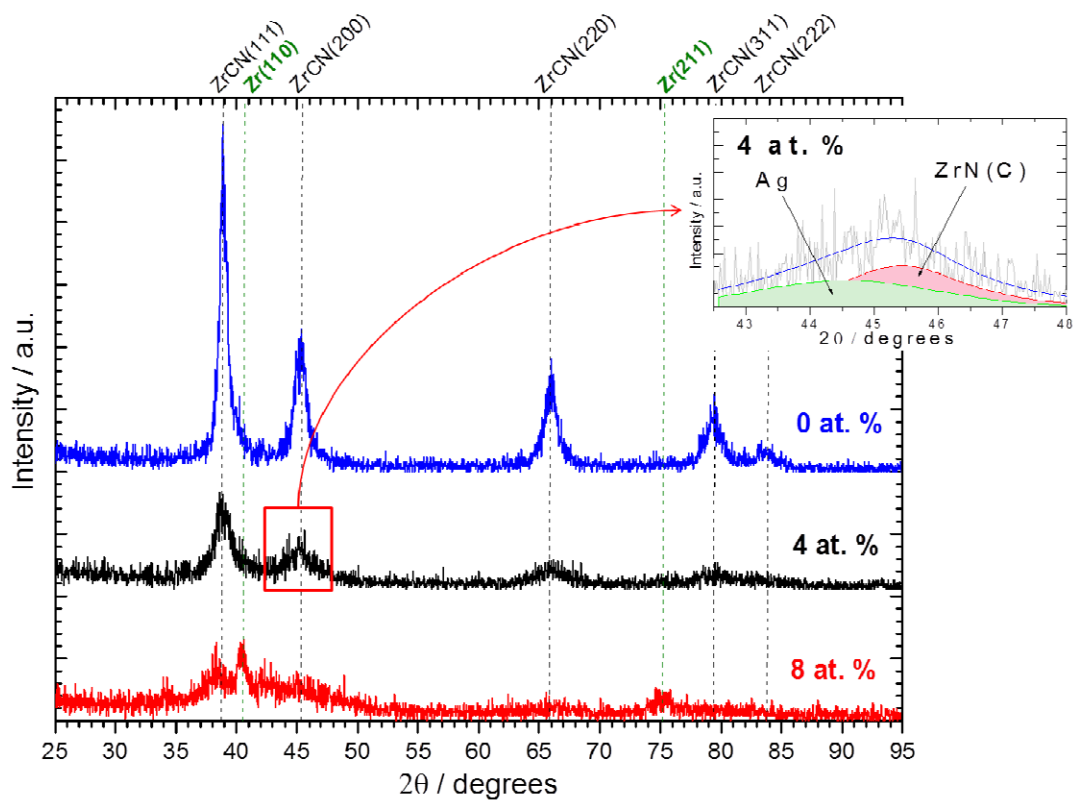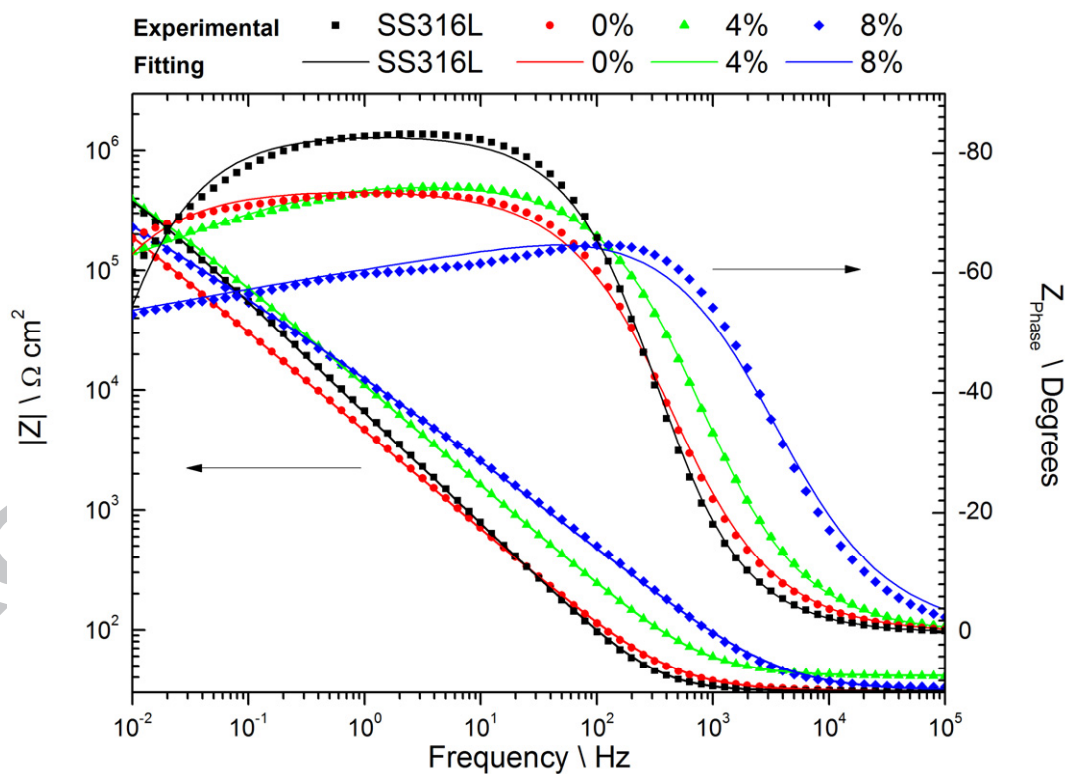
Highlights

- Zr-C-N-Ag coatings were produced by unbalanced magnetron sputtering.
- Ag alters the structure of the films, inducing lower grain sizes and a: C phases.
- Clear dependence of the R_p and C_{eff} of the films on the silver content is found.
- Films with low Ag at. % improve the corrosion resistance of the uncoated SS316L.